Predicting photoemission intensities and angular distributions with real-time density-functional theory

M. Dauth and S. Kümmel
Theoretical Physics IV, University of Bayreuth, D-95440 Bayreuth, Germany
(Received 11 December 2015; published 2 February 2016)

Photoemission spectroscopy is one of the most frequently used tools for characterizing the electronic structure of condensed matter systems. We discuss a scheme for simulating photoemission from finite systems based on time-dependent density-functional theory. It allows for the first-principles calculation of relative electron binding energies, ionization cross sections, and anisotropy parameters. We extract these photoemission spectroscopy observables from Kohn-Sham orbitals propagated in real time. We demonstrate that the approach is capable of estimating photoemission intensities, i.e., peak heights. It can also reliably predict the angular distribution of photoelectrons. For the example of benzene we contrast calculated angular distribution anisotropy parameters to experimental reference data. Self-interaction free Kohn-Sham theory yields meaningful outer valence single-particle states in the right energetic order. We discuss how to properly choose the complex absorbing potential that is used in the simulations.

DOI: 10.1103/PhysRevA.93.022502

I. INTRODUCTION

Outer valence electrons determine a wide range of properties inherent to condensed matter systems that are relevant to physics, chemistry, and material science. A fundamental understanding of these properties can often be gained by analyzing the valence electrons' density of states. The primary technique for determining the density of states is photoemission spectroscopy (PES) [1]. With PES' growing sophistication, increasingly detailed insights have become possible. Even the spatial structure of outer valence molecular orbitals could recently be revealed by techniques such as angular resolved photoemission spectroscopy (ARPES) [2–8] and high-harmonic generation [9–12]. Yet, theoretically predicting photoemission observables with satisfying accuracy is still challenging for state-of-the-art computational methods. Density-functional theory (DFT) is one of the most frequently used electronic structure approaches because it offers a favorable ratio of computational cost to accuracy. The customary approach for predicting photoemission spectra from DFT calculations is to approximate ionization potentials (IPs) by Kohn-Sham (KS) or generalized KS eigenvalues from self-consistent ground-state calculations [13–17]. This is based on the—in exact DFT rigorously valid—relation that the highest occupied molecular orbital (HOMO) eigenvalue equals the first ionization potential [18–21]. In addition to this rigorous relation it has been demonstrated that exact KS eigenvalues can be decent approximations to higher IPs of outer valence electrons, with deviations to experiment on the order of 0.1 eV [22]. Furthermore, KS eigenvalues are connected to quasiparticle energies by a perturbation expansion in which the former are the leading contribution [17,22].

In practice the predictive power of DFT eigenvalues strongly depends on the approximation for the exchange-correlation (xc) functional that is used. Known deficiencies of common functionals, in particular with respect to an accurate description of photoemission, are for instance the self-interaction error (SIE), the absence of a derivative discontinuity, and the deviation from the correct asymptotic $\sim -1/r$ behavior of the xc potential [19,20,23–28]. Yet, it has been demonstrated that, e.g., tuned-range separated hybrid functionals can predict IPs with an accuracy that matches that of many-body perturbation theory methods such as the *GW* approximation [26,29].

While ground-state DFT can thus make relevant contributions to the understanding of PES experiments, there are also important characteristics of PES spectra that cannot be captured by ground-state DFT for fundamental reasons. Dynamical effects such as the interaction of the ejected photoelectron with the remaining system are intrinsically beyond a ground-state approach. Furthermore, the "static eigenvalue approach" gives information about the relative photoemission intensities, i.e., the ratio of ionization cross sections at different binding energies, only in a very approximate way. For understanding this problem, one should recall that in a single-particle picture, the ionization cross section follows from Fermi's golden rule under the assumption that one electron is ejected from a specific single-particle orbital φ_i. However, calculating PES intensities from transition matrix elements (including the dipole operator $\mathbf{Ap}$),

$$I \propto |\langle\psi_k|\mathbf{Ap}|\varphi_i\rangle|^2 \delta(E_{\mathrm{kin}} + \hbar\omega - \epsilon_i), \tag{1}$$

requires knowledge about the state of the emitted electron ψ_k. Finding a reliable approximation for this photoelectron wave function is a delicate task. Furthermore, using DFT orbitals in the evaluation of matrix elements assigns physical meaning to the orbitals, which rigorously taken are just auxiliary quantities. Hence, one usually does not explicitly evaluate any matrix element at all, but simply ascribes a normalized intensity to each eigenvalue [13,14,17,26,29,30]. With this simplistic approach the relative peak heights in a spectrum are determined just by the degeneracy of the eigenvalues. Investigating PES with time-dependent DFT (TD-DFT) in the linear response limit allows for including some dynamical effects, but also does not lead to a rigorous assessment of emission intensities [31–33].

Constructing (approximate) Dyson orbitals from KS Slater determinants [34,35] is yet another way of going beyond the purely static picture, but leads to a different level, both

conceptually and in terms of computational complexity. In this work, we discuss a way to evaluate PES observables directly from TD-DFT. In this way, dynamical effects, if desired also beyond the linear regime, are explicitly taken into account (Sec. II). We further show in Sec. III that one can obtain reasonable estimates for intensity heights and binding energies. Finally we demonstrate in Sec. IV that the approach is able to predict the angular distribution of photoelectrons. Conclusions and an outlook are offered in Sec. V.

II. PHOTOEMISSION FROM REAL-TIME PROPAGATION

When one wants to take into account the dynamical nature of the PES process and wants to assess PES intensities, it is natural to go over to an explicitly time-dependent description. TD-DFT [36] allows for realizing this idea by propagating a system's occupied KS orbitals in real time and real space using the time-dependent KS equations [32,36–40]. This ansatz is particularly interesting as the entire dynamics, *including* the dynamics of the ionized density, is captured. The key question, however, is how to obtain photoemission observables from the time-dependent electron density. By virtue of the Runge-Gross theorem [36], the existence of a density functional for the ionization probability is guaranteed, but so far an exact, explicit functional form has not been discovered. However, different approximate schemes have been suggested [32,41–44].

Giovannini *et al.* proposed a photoelectron density functional relying on a phase-space interpretation of photoemission [41]. At the heart of this method lies a Wigner transformation of the TD KS density matrix. It has been interpreted as an approximate, semiclassical probability distribution for finding a photoelectron with a certain momentum at a certain point in space.

An alternative approach that is attractive because of its transparency was suggested by Pohl *et al.* [42,45,46]. One records the occupied orbitals at a detection point $\mathbf{R}_\mathrm{D}$ as a function of time, i.e., one records $\varphi_j(\mathbf{R}_\mathrm{D},t)$ for $j = 1,\ldots,N$, where N is the number of electrons. Each orbital can be interpreted as being a superposition of plane waves, i.e., $\varphi_j(\mathbf{R}_\mathrm{D},t) = \int d\omega\, c_j(\omega) \exp[i(\mathbf{k}\mathbf{R}_\mathrm{D} - \omega t)]$. For R_D far away from the system, this superposition can be interpreted as an outgoing wave packet. Consequently, a Fourier transform of $\varphi_j(\mathbf{R}_\mathrm{D},t)$ from the time into the frequency domain reveals $|c_j(\omega)|^2$ as the probability with which a certain kinetic energy is found in the outgoing wave packet. Summing over all orbitals yields the total probability density for detecting the kinetic energy E_kin at space point $\mathbf{R}_\mathrm{D}$,

$$n(\mathbf{R}_\mathrm{D}, E_\mathrm{kin}/\hbar) = \sum_{i=1}^{N} |\varphi_i(\mathbf{R}_\mathrm{D}, E_\mathrm{kin}/\hbar)|^2 = \sum_{i=1}^{N} |c_i(E_\mathrm{kin}/\hbar)|^2, \quad (2)$$

which is proportional to the probability of finding a photoelectron with kinetic energy E_kin at space point $\mathbf{R}_\mathrm{D}$, i.e.,

$$I(\mathbf{R}_\mathrm{D}, E_\mathrm{kin}) \propto n(\mathbf{R}_\mathrm{D}, E_\mathrm{kin}/\hbar). \quad (3)$$

Equations (3) and (2) define an implicit density functional for the photoemission intensity. It avoids interpreting the eigenvalues as removal energies, which is satisfying from a formal DFT perspective. A second and important advantage is that no *a priori* assumptions about the outgoing electron's (final) state have to be made—the outgoing electron's state emerges naturally during the propagation. A third advantage is that the scheme is ideally suited for obtaining the spatial distribution of emitted electrons by placing detection points on a spherical surface around the probed molecule (see the discussion further below).

On the fundamental level, there is one inherent approximation made in the derivation of Eqs. (3) and (2): By interpreting the TD KS orbitals at large R_D as outgoing wave packets, one implicitly identifies KS particles with electrons. A second approximation—inherent to almost all (TD-)DFT calculations—is of course that one has to rely on an approximate exchange-correlation functional. These two issues are somewhat related: Because the scheme identifies KS particles with electrons, it is clear that it can be expected to work best with exchange-correlation approximations that conform with this identification. The self-interaction correction (SIC) [47] used as a KS scheme meets this criterion, as discussed in Refs. [48,49].

In practice there is a third set of approximations which are of purely technical nature, but nevertheless very important. These are related to the choice of the detection point and the boundary conditions that are used in the simulation. The detection point $\mathbf{R}_\mathrm{D}$ should be placed as far as possible from the system's center to ensure that one only analyzes density that corresponds to detached electrons. Thus, the real-space grid on which we run our simulations should be chosen as large as possible (see Appendices A and B). A second reason for choosing a large grid is related to the boundary conditions: In order to prevent that outgoing density is reflected back when it reaches points on the grid boundaries (R_b) and interferes with outgoing waves, we do not use the zero boundary condition that is used in ground-state calculations [$\varphi(R_\mathrm{b}) = 0$]. Instead we employ an imaginary absorbing potential [50,51]. In doing so it is important that the absorbing function is chosen to be very smooth and that the effective absorbing region is large enough to absorb all Fourier components of the outgoing wave packet [51]. These conditions can be fulfilled easier, the larger the grid is. Yet, the computational effort grows noticeably with increasing grid size, and one therefore has to optimize the numerical setup to obtain good accuracy at reasonable computational expense. We acquire our PES signals (as, for instance, displayed in Figs. 2 and 3) according to Eq. (3) without substantial numerical noise for benzene and pyridine by using a spherical simulation box with a radius of $R_\mathrm{b} = 24a_0$ and an exponential function for the absorbing potential, which we add to the usual KS Hamiltonian (see Appendix A). The detection points have to be placed in a region where the absorbing potential is still small and the molecule's potential has (sufficiently) faded. We found that in the present calculations a radius of $R_\mathrm{D} = 17.5a_0$ was a good choice. We further note that the potential created by the ionizing light is present at the detection point. As we use only moderate intensities of $8.8 \times 10^7 \mathrm{W/cm^2}$, we assume its impact to be small [43]. In Appendix A we discuss in detail how the the choice of R_D affects the spectra.

III. GAS-PHASE PHOTOEMISSION FROM BENZENE AND PYRIDINE

In gas-phase photoemission spectroscopy the probed ensemble of molecules is confined in a cavity and the molecules are randomly oriented. The photoemission process is triggered by linear polarized light with a fixed photon energy, here $\hbar\omega = 21.2$ eV, incoming from a certain direction [1,52,53]. In order to simulate this experimental situation, we cannot restrict ourselves to one TD-DFT simulation run, because one run corresponds to one distinct alignment of the molecule with respect to the light polarization. To average over the different molecular orientations as in experiment, we simulate different alignments in separate runs. Instead of varying the molecule's orientation towards the fixed light polarization it is computationally more convenient (and equivalent) to keep the molecule fixed and to rotate the linear light polarization. We place the benzene, respectively, pyridine, ring in the x-y plane and sample over the polarization directions as illustrated (for the first octant) in Fig. 1. The polarization directions for the other octants are completely equivalent. Thus, due to the symmetry of benzene, we can reduce the number of actually needed TD-DFT runs to the ones displayed.

We compute the angle-integrated cross section for one single TD-DFT run by distributing about 3000 detection points on a spherical surface with radius R_D and by integrating over all individual intensities from the detection points.

In the first step of our analysis we focus on binding energy differences between the outer valence states. In order to obtain these reliably it is essential to correct for the self-interaction error that is present in commonly used xc functionals [5,24,25]. Therefore, we use the KS SIC, respectively, time-dependent SIC (TD-SIC) [48,49,54,55]. It is based on the seminal SIC energy functional of Perdew and Zunger [47]. However, contrary to the orbital-specific potential approach of Ref. [47], we here stay on the grounds of KS theory and construct a local multiplicative xc potential using the time-dependent [56] generalized [54] Krieger-Li-Iafrate [57] (TD-GKLI) approximation to the optimized effective potential equation with a complex Foster-Boys localizing unitary orbital transformation [49].

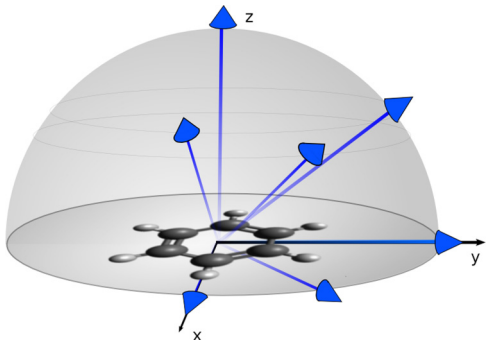

FIG. 1. Blue arrows indicate the seven different directions of the light polarization that were chosen to simulate the angularly averaged photoemission spectrum of the benzene molecule. In the chosen coordinate system shown in the figure, the polarization directions indicated by the blue arrows correspond to the vectors (1,0,0), (0,1,0), (0,0,1), (1,1,0), (1,1,1), (0,1,1), and (1,0,1).

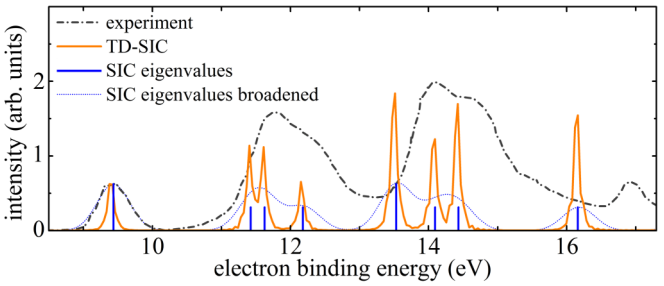

FIG. 2. Photoemission spectrum of benzene. Black dashed line: Experimental spectrum from Ref. [52]. Orange full line: Photoemission spectrum as predicted by TD-SIC. Dotted blue line: Ground-state SIC eigenvalues folded by Gaussian functions with a width of 0.4 eV. Blue bars indicate the positions of the SIC eigenvalues. The peak position and height at the smallest binding energy were scaled to match the corresponding experimental peak for all theoretical spectra.

Figures 2 and 3 show the resulting PES spectra for benzene and pyridine, respectively. In order to facilitate comparison with the experimental data we aligned all calculated eigenvalues and the spectrum obtained from the TD calculation such that the first peak in the theoretical spectra in each case coincides with the first experimental peak [58]. Consequently, we restrict our analysis to relative energy differences.

For benzene, the (shifted) first ground-state SIC eigenvalue corresponds to a binding energy of $E_B = 9.4$ eV, and the second eigenvalue corresponds to $E_B = 11.4$ eV. Their difference matches the difference between the first two experimental peaks reasonably well, deviating by 0.3 eV. Altogether, three eigenvalues are correctly found within the experimental emission band around $E_B \approx 12$ eV [26,59]. The next (lower) three eigenvalues (close to $E_B \approx 14$ eV) are located at slightly too low binding energies. The reason for discrepancies of this kind has been clarified in earlier work: KS eigenvalues are just lowest order approximations to ionization potentials, and higher order corrections lead to an effective "stretching" of the spectrum [17,22]. Nonlocal exchange can correct KS eigenvalues towards quasiparticle energies [15,17,22,26]. The same effect is seen even more pronouncedly for the eigenvalue at $E_B \approx 16$ eV.

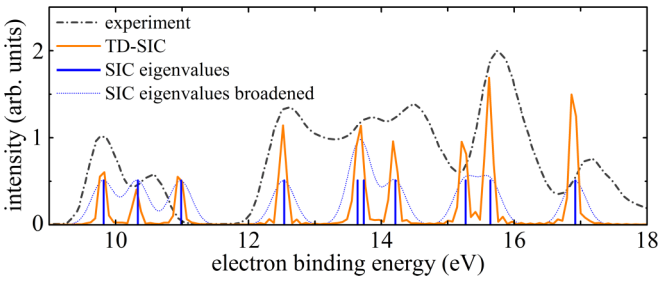

FIG. 3. Photoemission spectrum of pyridine. Black dashed line: Experimental spectrum from Ref. [52]. Orange full line: Photoemission spectrum as predicted by TD-SIC. Dotted blue line: Ground-state SIC eigenvalues folded by Gaussian functions with a width of 0.4 eV. Blue bars indicate the positions of the SIC eigenvalues. The peak position and height at the smallest binding energy were scaled to match the corresponding experimental peak for all theoretical spectra.

When we now turn towards the time-dependent description of PES by the real-time approach, our first observation is that the energetic positions of the PES intensities do not change significantly: The orange peaks are almost at the same positions as the blue lines that mark the eigenvalues. This shows that, at least with the chosen xc approximation, the positions of the photoemission peaks are primarily determined by the ground-state electronic structure and are hardly affected by dynamical interactions.

However, despite the similarity in the peak *positions*, the peak *heights* that are obtained in the time-dependent calculation differ significantly from the peak heights predicted by the ground-state calculation. In order to ease the comparison between the experimental data and the different calculations, we scaled the theoretical intensities plotted in Fig. 2 such that the peak height at the smallest binding energy in each case equals the height of the first experimental peak. Looking at the blue dotted curve that reflects the eigenvalue-based prediction for the intensities then shows that for the larger binding energies, i.e., for the three peaks around 12 eV and for the three around 14 eV, the intensity is severely underestimated: Based on the eigenvalues' degeneracies one would expect the peaks at 12 and 14 eV to have approximately the same heights as the first peak at 9.4 eV. Yet, in the experimental spectrum, the peaks around 12 and 14 eV are more than twice as high as the first peak.

This serious deficiency is to a large extent remedied when the photoemission spectrum is calculated with the real-time approach. The orange line that reflects the intensity from the TD-DFT calculation shows the same pattern of increasing peak heights as the experiment and captures the relative heights of the first three main emission bands (around $E_B \approx 9.4$, 12.0, and 14.0 eV) well. That this is a nontrivial finding is seen particularly well when looking at the TD-DFT peaks at binding energies of $E_B \approx 9.4$ eV and $E_B \approx 13.5$ eV (see Fig. 2). Both correspond to doubly degenerate Kohn-Sham states, yet the intensities from the TD-DFT calculation differ by a factor of about 3. Thus, in the real-time approach it is not the degeneracy that governs the intensity, but the dynamics and final state effects. TDDFT thus captures effects that are intrinsically beyond a ground-state-based interpretation of photoemission and leads to a much better agreement with the experimental observation.

Finally, we note that deviations between experiment and the real-time results occur for the emission peaks corresponding to more strongly bound electrons (from 16 eV onwards for benzene, from 17 eV onwards for pyridine, not shown in the figures). In an orbital-based interpretation, the origin of these peaks can be traced back to the HOMO-9 and further down. Whether these discrepancies are a consequence of the employed xc approximation or of the implicit identification of KS particles with electrons remains to be investigated in future work.

Similar findings as the one just discussed for benzene are also made for other systems, e.g., pyridine, as shown in Fig. 3. Again we display the binding energies as obtained from the eigenvalues and as found in the real-time approach (both rigidly shifted by $\Delta = 2.8$ eV). Again the relative energetic positions found in the two approaches are very similar and are overall in good agreement with experiment. The positions of emission peaks above $E_B = 12$ eV are even closer to the experimental reference than for the case of benzene. We note, however, that the first two peaks around $E_B = 10$ eV should be quasidegenerate [26,59], i.e., the separation of about 0.4 eV that we find here is too large. This affects the scaling of the theoretical spectra, which we again want to do such that the first peak height matches the first experimental peak height. We account for the overestimation of the peak separation by scaling the added intensities of the first two calculated peaks to the first experimental peak height. With a common basis for the comparison of relative peak heights thus established, it becomes obvious that the ground-state eigenvalue approach (blue line in Fig. 3) again considerably underestimates the intensity of the emission peaks that correspond to binding energies of about 12 eV and more. Yet, as in the case of benzene, the real-time approach cures this deficiency and predicts considerably higher intensity for the more strongly bound electrons, in agreement with experiment. As a specific example one may look at the emission peaks at about $E_B = 12.5$ and 15.7 eV: The considerable increase in intensity that is seen in the experiment is well reproduced by the real-time approach, yet missed completely by the eigenvalue-based interpretation of photoemission. We thus conclude that the real-time approach to photoemission can capture what commonly is called "matrix element effects" [31] without explicitly evaluating any matrix elements.

IV. ORBITAL CHARACTERIZATION

Photoemission can reveal much more about a system's electronic structure than what can be inferred from peak positions and peak heights. Of particular interest is the spatial distribution of the electronic density. Measurements that have been interpreted as showing single-particle orbitals or orbital densities, respectively, have become possible with the techniques of high-harmonic generation [9–12] or ARPES [2–5,7,8]. However, the number of systems which can be studied in this way is limited for various reasons. ARPES, e.g., requires an aligned molecular monolayer to prevent averaging over emission directions. This restricts the repertory of molecules that can be studied. Although gas-phase PES provides no immediate access to data that can be interpreted as reflecting orbitals, such information can be extracted from the specific emission behavior at different binding energies. When one realizes PES without any preferred direction, the photoelectron angular distribution from a randomly oriented ensemble is strictly uniform. Yet, one can take advantage of the typical gas-phase PES experimental setup that has one distinguished direction, namely, the spatially fixed linear light polarization. As a result the photoemission intensity can vary with respect to the polarization direction. If one defines θ as the angle between the photoelectron emission direction and the light polarization ($\theta = 0^\circ$ and $\theta = 180^\circ$ parallel; $\theta = 90^\circ$ perpendicular), the photoemission intensity for spherical systems is given by [45,60–62]

$$I(E,\theta) \propto 1 + \beta(E) P_2(\cos\theta). \tag{4}$$

Here, P_2 is the Legendre polynomial of second order. The angular dependence (i.e., deviation from a spatially uniform emission) introduced by $P_2(\cos\theta)$ is weighted by

the factor β, called the anisotropy parameter. The largest possible value of the anisotropy parameter, determined by dipole selection rules [60], is $\beta = 2$. It corresponds to an emission maximally parallel to the light polarization with $I(\theta) \propto \cos^2\theta$. An emission that is primarily perpendicular to the polarization is indicated by $\beta = -1$, which leads to $I(\theta) \propto \sin^2\theta$.

Typically, individual photoemission bands show different emission characteristics, and β can vary between the two limiting cases. When the photoemission signal is interpreted in terms of molecular orbitals, i.e., when each emission peak is assigned to electron ejection from one specific orbital as in Eq. (1), the variation in β as a function of energy can be ascribed to probing different molecular orbitals with different spatial structure. However, there is another ingredient to the transition matrix element in Fermi's golden rule in Eq. (1), namely, the final state of the ejected electron. It can also affect the emission characteristics. A direct evaluation of Fermi's golden rule was, for example, realized by approximating the photoelectron's state with the aid of multiple scattering X_α approaches [53,63]. However, the real-time propagation approach is an elegant and parameter-free way to bypass the need for explicitly specifying the ejected electron's state. It allows for connecting orbitals and emission peaks in an unbiased way. Separately evaluating the emission from the individual orbital densities $n_i(E)$ as discussed in Sec. II, then calculating $\beta_i(E)$ and comparing these values to the anisotropy parameters that were experimentally recorded for the individual emission bands, allows us to check the *orbital assignment* in a straightforward way. Closely linked to the orbital assignment question is the finding that different xc-functional approximations can predict different orbital orderings [5,17,24,64]. This raises the question of which theoretical approach gives the "correct" energetic ordering of orbitals. The self-interaction error plays a prominent role in determining the orbital ordering [24]. In the following we show that anisotropy parameters calculated for individual emission peaks based on the KS SIC orbital ordering match the experimentally measured anisotropy parameters well.

To calculate the anisotropy parameter for benzene, we record, similar to Wopperer *et al.*, who calculated β for sodium clusters [45,46], the PES signal angle and energy resolved. We again use the alignment scheme for the gas-phase PES calculation from Sec. III including the variation of the light polarization instead of the molecule's orientation. However, a smooth angular signal requires a denser discretization of light polarization to molecule alignment directions. Furthermore, we have to transform all individual spectra from the molecular frame (with the spatially fixed molecule and varying light polarization) into the laboratory frame where the light polarization is spatially fixed, i.e., is pointing into the z direction. Afterwards we sum the individual spectra up to obtain the total, angle-resolved photoemission spectrum. As the only distinguished direction is that of the light polarization, we integrate the intensity over the azimuthal angle which lies in planes perpendicular to the light polarization (in the laboratory frame). We provide further details regarding the calculation of β in Appendix C.

Figure 4 shows two examples for the resulting angle-resolved emission intensity for the case of benzene. The left panel depicts the angle-resolved emission intensity solely from the two degenerate HOMOs. Thus, instead of taking the entire electron density into account as in Eq. (3), we exclusively calculated the intensity ejected from the HOMOs, $I_{\mathrm{HOMO}} \propto n_{\mathrm{HOMO}}$. This angle-resolved signal was evaluated at the HOMOs' electron binding energy. A polar angle θ equal to 0° or 180° indicates emission parallel to the light polarization (marked by the arrows in Fig. 4). We have fitted the intensity profile of the calculated data according to Eq. (4). The resulting β value amounts to $\beta = 0.75$, which indicates an emission primarily towards the polarization direction. As an example for perpendicular emission we show in the right part of Fig. 4 the angle-resolved intensity profile which corresponds to the most negative anisotropy parameter, $\beta = -0.20$ (this value corresponds to the emission at $E_{\mathrm{B}} = 14.6$ eV in Fig. 5).

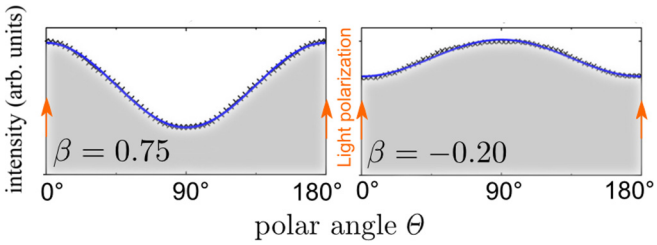

FIG. 4. Left: Angle-resolved photoemission intensity from the benzene HOMO as predicted by TD-SIC. The direction of the light polarization is indicated by the orange arrows. Photoemission parallel to the light polarization corresponds to $\theta = 0°$ and 180°; $\theta = 90°$ corresponds to perpendicular emission. The calculated intensity (black crosses) was fitted with the help of Eq. (4), resulting in $\beta = 0.75$ (blue line). Emission occurs predominantly parallel to the light polarization. Right: Angle-resolved photoemission intensity from the benzene HOMO-7 (green-white orbital in Fig. 5). Here the emission is predominantly perpendicular to the light polarization, with $\beta = -0.20$.

Figure 5 shows the shapes of the benzene orbitals at the very top, in the upper panel the experimentally recorded β values for benzene from Refs. [52,53,65,66], and the measured and calculated photoemission spectra in the lower panel. In order to compare measured and calculated β values in a meaningful way, the scales for the binding energies must match. Therefore, we enhance the resemblance of the two spectra by stretching the calculated spectrum by a constant factor of $s = 1.11$. With this stretching factor, the first (lowest binding energy) and last (highest binding energy) calculated peak in Fig. 5 coincide exactly with the corresponding experimental peaks. This *a posteriori* stretching procedure can be understood as imitating a first order correction of the KS eigenvalues towards quasiparticle energies [17,22].

We now discuss the data going through the spectrum, starting at the lowest binding energy of 9.4 eV. For this first peak we calculated $\beta = 0.75$, as indicated by the leftmost triangle in the upper panel of Fig. 5. We see that the experimentally measured values of β in this energy range show quite some scatter, but are generally of quite similar magnitude (though the theoretical value admittedly lies at the lower end of the experimental scatter). Going to higher binding energies the experimental emission characteristic changes significantly

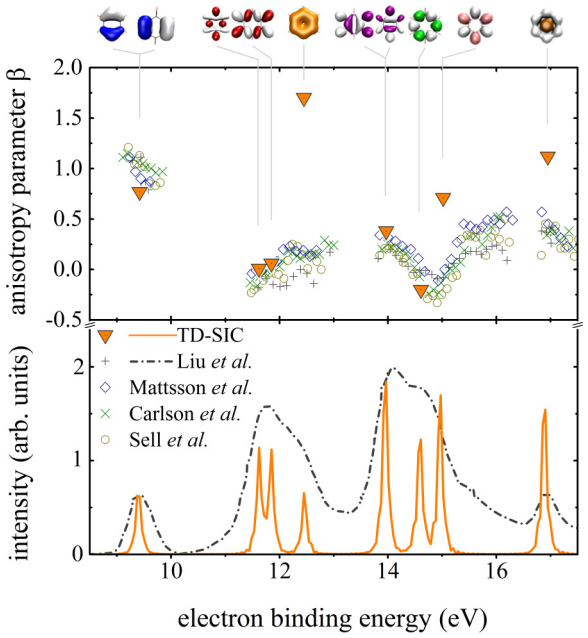

FIG. 5. Lower panel: Experimentally recorded photoemission spectrum for benzene from Ref. [52] (black) and photoemission spectrum from TD-SIC (orange). In difference to Fig. 2, we here stretched the theoretical spectrum by a factor of $s = 1.11$ to ease comparison to experiment. Top panel: Anisotropy parameter β as a function of energy. Triangles depict the calculated values obtained for the emission from individual orbitals, i.e., corresponding to the peaks shown right below in the lower panel. Different experimental β values are designated by small symbols as designated in the plot, with the data taken from Liu *et al.* [52], Carlson *et al.* [53], Mattsson *et al.* [65], and Sell and Kuppermann [66].

and becomes uniform, with values of β that are close to zero. This is correctly reflected by the TD-DFT calculation, which yields $\beta = 0.01$ at $E_B = 11.7$ eV. Similar, the transition of β from positive over slightly negative and back to positive values in the binging energy region from 14.0 to 15.5 eV is accurately reproduced. This characteristic transition enables a decomposition of the rather broad emission band in terms of the origins of the photoelectrons. As we obtained the β values from the individual orbital densities separately, it allows us to draw conclusions about the responsible orbitals, as indicated at the top of Fig. 5.

The only severe discrepancy between theory and experiment is seen for the anisotropy parameter at $E_B = 12.2$ eV. It corresponds to the π orbital that is completely delocalized over the whole benzene ring. While the calculated value of $\beta = 1.70$ suggests an electron emission mostly along the polarization, measurements observe a rather uniform electron emission. A possible explanation is the natural broadening of the emission peaks. The only sparsely pronounced shoulder at around $E_B = 12.5$ eV testifies a strong mixing of the emission from the neighboring states with the ring-shaped one. Probably, the experimental anisotropy parameter is thus notably suppressed by the nearby states showing a uniform emission with $\beta = 0.01$. Moreover, the ring orbital is predicted to be slightly overbound by SIC, most likely due to a lack of beyond (semi-)local correlation [26]. It thus should be even closer to the states with the next lower binding energy than seen in our spectrum in Fig. 5. We are therefore inclined to believe that the value of β which we calculated for the ring orbital and find to be noticeably larger than zero, is not an artifact. Yet, the precise theoretical value may be influenced by electron-electron interaction effects that are beyond our xc-functional approximation, and the experimental data may suffer from orbital near degeneracy. Therefore, we presently cannot draw a final conclusion.

Yet, the overall agreement between theory and experiment for β is quite good, and we can therefore return to the question of assigning orbitals to emission peaks. Since the orbital is a noninteracting particle concept, while true electrons are interacting, this assignment is of course an approximation. However, in line with the results of Carlson *et al.* [53] our results confirm that, at least for the present systems, the interpretation that individual emission bands stem from individual orbitals is a reasonable one and is confirmed by the directional-specific emission behavior. Along with earlier works on the interpretability of molecular orbitals [2,5,22,34,67,68] we can further corroborate the assertion that KS orbitals can be attributed physical significance, i.e., KS orbitals have more meaning than just being auxiliary quantities that reproduce the electron density.

V. CONCLUSION

We simulated photoemission from organic molecules using self-interaction-free KS TD-DFT. Doing so we go beyond the static, ground-state approach to photoemission which interprets the eigenvalues as ionization potentials and infers relative peak heights just from degeneracies. The TD-DFT approach explicitly includes dynamical effects and allows for the first-principles calculation of gas-phase PES with angular resolution. We demonstrated for benzene and pyridine that a strength of the approach lies in yielding reasonable estimates for photoemission intensities. This improvement is a consequence of including dynamical effects and of not relying on the evaluation of Fermi's golden rule which necessitates, e.g., an approximation for the ejected electron's state. The real-time approach makes a straightforward evaluation of PES intensities possible via Eq. (3). We have used the method for calculating angle-resolved photoemission from benzene. Assessing the photoemission anisotropy with respect to a spatially fixed light polarization, expressed in terms of the anisotropy parameter β, and comparing β values calculated for individual orbital emissions to measured values of β, showed that associating individual photoemission peaks with individual orbitals is a very useful concept for the systems studied here. We are convinced that this approach is promising also for other systems and applications. In particular, the description of situations which require one to go beyond stationary or simple final state approximations will benefit from the accurate, first-principles approach in which the final state emerges naturally without *a priori* assumptions. For example, the prediction of circular dichroism in the photoelectron angular distribution is a challenge in which we expect valuable contributions from our method.

ACKNOWLEDGMENTS

S.K. and M.D. acknowledge support by Deutsche Forschungsgemeinschaft Graduiertenkolleg 1640 and the Bavarian State Ministry of Science, Research, and the Arts for the Collaborative Research Network "Solar Technologies go Hybrid".

APPENDIX A: DETECTION POINT DEPENDENCE

In this section, we discuss details of our technical setup regarding the choice of the absorbing potential and the detection point. These are rather technical issues. They are important, however, because the interplay of quite a number of factors is important for obtaining reliable results with bearable computational effort. Among the things that one has to take into account are the choice of the detection point, the choice of the shape of the absorbing imaginary potential, its strength, the radial extension of the volume in which the absorbing potential acts, and the size of the simulation box (which one would like to be as small as possible to minimize the computational effort).

We start by discussing the absorbing potential. As stated in Sec. II we have chosen an exponential function,

$$-i\,v(r) = -i\,\exp\frac{r - R_\mathrm{b}}{1.39a_0}. \tag{A1}$$

We tested several other potential shapes. Polynomial functions of second order and transmission-free absorbing potentials [51] led to similar results, but overall we found that the potential of Eq. (A1) performed best. It has the advantage of being continuous and very smooth, thus being very unlike a steplike structure that causes quantum-mechanical reflections. However, the price that has to be paid is that the potential is not vanishing at any point in the simulation box. Therefore, it in principle absorbs some probability density also in the central molecular region. However, this amount can be kept extremely small in practice and utterly negligible with a proper choice of parameters. In our experience it is mainly the effective length (effective absorbing region) that is crucial for efficiently absorbing all Fourier components (respectively, all wavelengths) of the outgoing density. In Fig. 6 we contrast three different effective absorption lengths, where the detection point was held fixed. We have changed the radius of the spherical numerical box from $R_\mathrm{b} = 24a_0$ to $22a_0$, and $20a_0$ and hence decreased the effective length of the potential according to Eq. (A1). This results in a dramatically increasing width

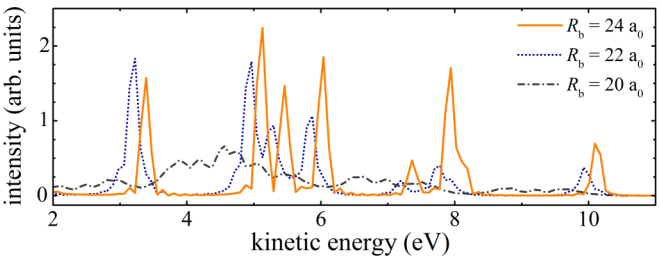

FIG. 6. PES spectra obtained using absorbing potentials with different effective length. We show the kinetic energy of photoelectrons from benzene for one relative orientation of light polarization and molecule.

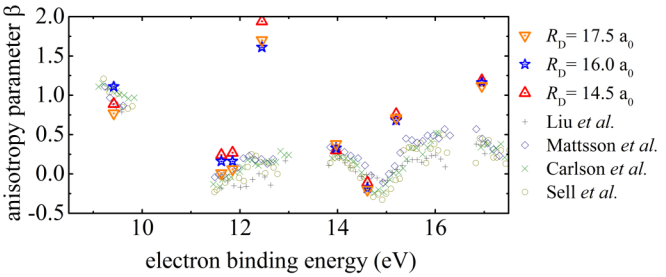

FIG. 7. Anisotropy parameter for three different choices of the detector radius: $R_\mathrm{D} = 14.5a_0$ (red triangles), $16.0a_0$ (blue stars), and $17.5a_0$ (orange triangles). Positions of the TD-SIC β values are aligned and scaled by $s = 1.11$. The experimental data is taken from Liu *et al.* [52], Carlson *et al.* [53], Mattsson *et al.* [65], and Sell and Kuppermann [66].

of the emission peaks as depicted in Fig. 6. Therefore, with decreasing effective absorption length the spectrum is increasingly contaminated by signals from quantum-mechanical reflections. An absorption region that is too small can easily wipe out the relevant signal.

The next parameter we discuss is the detection point R_D. For the potential (A1) with a box size of $24a_0$, we set R_D to $17.5a_0$, $16.0a_0$, and $14.5a_0$ [as measured from the center of the simulation box. For comparison: the H atom furthest away from the coordinate origin (the origin is also the center of mass of the benzene molecule) is located at $R \approx 4.7a_0$.]. To demonstrate the influence, we show the anisotropy parameters in Fig. 7 evaluated in exactly the same way as described in the main text in Sec. IV, just using the different values for R_D. The resulting differences are visible, but are not huge and lie within the experimental uncertainty range.

In contrast to the minor influence on the anisotropy parameter, the difference is more pronounced for the PES intensities, i.e., peak heights. Figures 8 and 9 show the PES spectra for benzene and pyridine for all three observation distances. Yet, we find moderate deviations in the intensity heights at, e.g., $E_\mathrm{B} = 13.5$ and 14.5 eV for benzene (Figs. 2 and 8).

Finally, we show the spectra that result without correcting for the one-electron SIE. The PES in Fig. 10 is evaluated in exactly the same way as for TD-SIC except for the difference in the xc approximation. We here used the local density approximation (LDA) which is strongly influenced by SIE. The TD-LDA PES spectrum does not resemble the experimental spectrum very much.

APPENDIX B: TECHNICAL DETAILS

For all our simulations we used the Bayreuth version of the PARSEC real-rime and real-space code [40,69], which uses norm-conserving Troullier-Martins pseudopotentials [70,71].

Our simulations for benzene and pyridine were performed with a grid spacing of $0.38a_0$ in the space and 0.001 fs in the time domain. The propagation time for benzene was 50 fs for the photoemission spectra and 25 fs for the TD-DFT runs necessary to calculate β. For pyridine we propagated the system for 30 fs. The ionizing laser pulse was simulated by a classical time-dependent electric field.

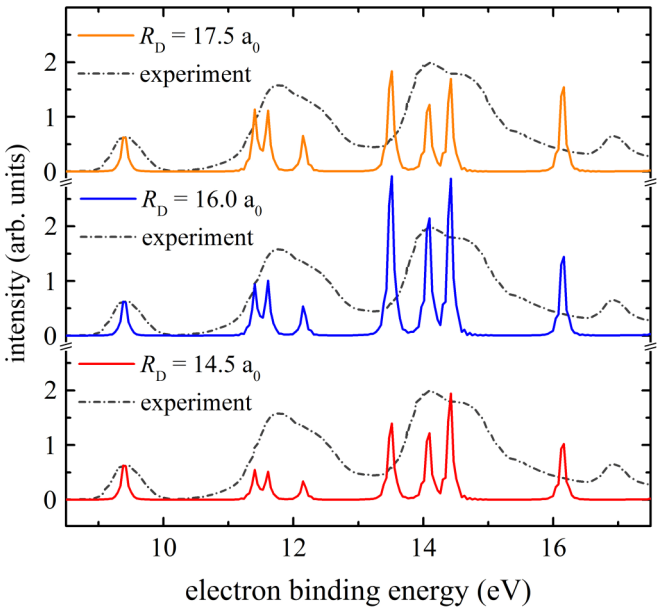

FIG. 8. Photoemission spectrum of benzene, predicted by TD-SIC, for three different choices of the detector radii: $R_D = 17.0a_0$ (orange), $16.0a_0$ (blue), and $14.5a_0$ (red). Experimental spectrum taken from Ref. [52].

This electric field was chosen as a sine with a frequency of $\hbar\omega = 21.2$ eV that was linearly ramped to its maximal intensity of $8.8 \times 10^7 \mathrm{W/cm^2}$ within 1 fs and then remained constant throughout the propagation time. The chosen spatial grid spacing is on the coarse side for the chosen elements and pseudopotentials. We went into this limit in order to keep the numerical burden for the time propagation with the TD-SIC approach manageable. (Changes in the real-space grid spacing relate approximately quadratically to the time step spacing, i.e., doubling the real-space grid spacing allows for

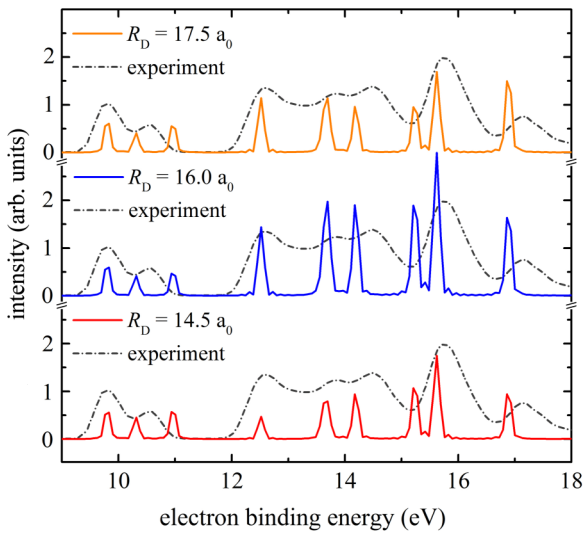

FIG. 9. Photoemission spectrum of pyridine, predicted by TD-SIC, for three different choices of the detector radii: $R_D = 17.0a_0$ (orange), $16.0a_0$ (blue), and $14.5a_0$ (red). Experimental spectrum taken from Ref. [52].

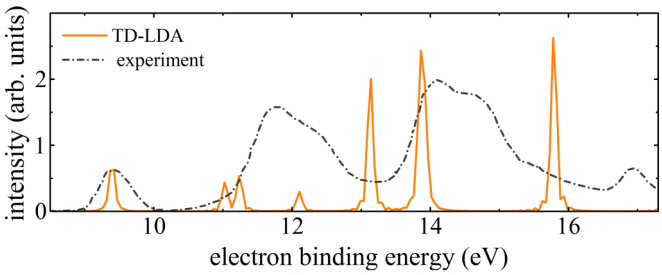

FIG. 10. Orange: Photoelectron spectrum of benzene as predicted by TD-LDA. Black: Experimental photoemission spectrum from Ref. [52]. The position and height of the TD-LDA peak corresponding to the smallest binding energy was aligned to its experimental counterpart. The agreement between TD-LDA and experiment is not good.

taking an about four times larger time step.). With respect to a calculation that uses a grid spacing that is tightened to convergence, the grid spacing of $0.38a_0$ leads to uncertainties in the eigenvalues of up to 0.2 eV. This tolerance is acceptable for the present purposes, but it does affect, e.g., the two benzene emission peaks at a binding energy of about 11.5 eV in Fig. 8. These are closer together when a smaller grid spacing is used. The convergence threshold for the localizing Foster-Boys unitary orbital transformation, which is described in Ref. [55], Eq. (B18), was set to 1×10^{-5}.

APPENDIX C: SAMPLING OF MOLECULE ORIENTATIONS

In order to calculate the intensity in a way that corresponds to experimental gas-phase PES setups, we need to sample over many molecule to light polarization directions. As discussed in Sec. IV, we varied the light polarization instead of the orientation of benzene (it lies in the x-y plane). The polarization vector directions—(1,0,0),(0,1,0), (0,0,1), (1,1,0), (1,1,1), (0,1,1), and (1,0,1)—are displayed in Fig. 1 and as red pentagons in Fig. 11 for the first octant in the case of benzene. In the case of pyridine, the nitrogen on one site of the ring lowers the symmetry compared to benzene.

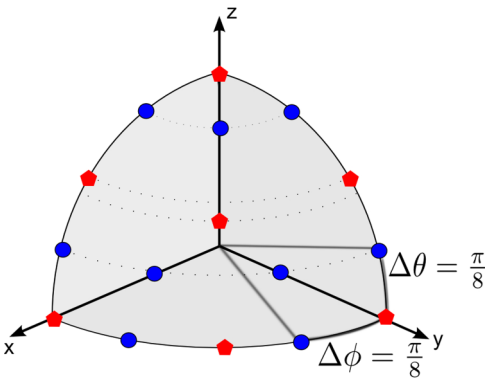

FIG. 11. Directions of the light polarization in the first octant with respect to benzene that is lying in the x-y plane. The red pentagons correspond to the directions chosen for calculating the PES spectra of benzene. For calculating β we additionally ran the TD-DFT simulations with the orientations corresponding to the blue dots.

To account for this, we additionally performed TD-DFT runs with the polarization orientations (1,−1,0) and (1,−1,1). The polarization directions for the octants that are not shown explicitly are analogous.

For recording the angular-resolved photoemission data for β from benzene we had to increase the number of discrete sampling directions in order to get a smooth angular signal. The additional polarization directions are displayed in Fig. 11 for the first octant. The polarization directions for the other octants are equivalent. The 16 directions for which we actually performed TD-DFT runs to calculate β are the ones shown in Fig. 11.

[1] S. Hüfner, *Photoelectron Spectroscopy* (Springer, Berlin, 2003), pp. 10–19.
[2] P. Puschnig, S. Berkebile, A. J. Fleming, G. Koller, K. Emtsev, T. Seyller, J. D. Riley, C. Ambrosch-Draxl, F. P. Netzer, and M. G. Ramsey, Science **326**, 702 (2009).
[3] S. Kera, S. Tanaka, H. Yamane, D. Yoshimura, K. K. Okudaira, K. Seki, and N. Ueno, Chem. Phys. **325**, 113 (2006).
[4] J. Ziroff, F. Forster, A. Schöll, P. Puschnig, and F. Reinert, Phys. Rev. Lett. **104**, 233004 (2010).
[5] M. Dauth, T. Körzdörfer, S. Kümmel, J. Ziroff, M. Wiessner, A. Schöll, F. Reinert, M. Arita, and K. Shimada, Phys. Rev. Lett. **107**, 193002 (2011).
[6] D. Lüftner, T. Ules, E. M. Reinisch, G. Koller, S. Soubatch, F. S. Tautz, M. G. Ramsey, and P. Puschnig, Proc. Natl. Acad. Sci. USA **111**, 605 (2013).
[7] M. Wießner, D. Hauschild, C. Sauer, V. Feyer, A. Schöll, and F. Reinert, Nat. Commun. **5**, 4156 (2014).
[8] S. Weiß, D. Lüftner, T. Ules, E. M. Reinisch, H. Kaser, A. Gottwald, M. Richter, S. Soubatch, G. Koller, M. G. Ramsey, F. S. Tautz, and P. Puschnig, Nat. Commun. **6**, 8287 (2015).
[9] J. Itatani, J. Levesque, D. Zeidler, H. Niikura, H. Pépin, J. C. Kieffer, P. B. Corkum, and D. M. Villeneuve, Nature (London) **432**, 867 (2004).
[10] B. K. McFarland, J. P. Farrell, P. H. Bucksbaum, and M. Gühr, Science **322**, 1232 (2008).
[11] S. Haessler, J. Caillat, W. Boutu, C. Giovanetti-Teixeira, T. Ruchon, T. Auguste, Z. Diveki, P. Breger, A. Maquet, B. Carré, R. Taib, and P. Salieres, Nat. Phys. **6**, 200 (2010).
[12] M. Lein, J. Phys. B **40**, R135 (2007).
[13] N. Binggeli and J. R. Chelikowsky, Phys. Rev. Lett. **75**, 493 (1995).
[14] J. Akola, M. Manninen, H. Häkkinen, U. Landman, X. Li, and L.-S. Wang, Phys. Rev. B **62**, 13216 (2000).
[15] L. Kronik, T. Stein, S. Refaely-Abramson, and R. Baer, J. Chem. Theory Comput. **8**, 1515 (2012).
[16] U. Salzner and R. Baer, J. Chem. Phys. **131**, 231101 (2009).
[17] T. Körzdörfer and S. Kümmel, Phys. Rev. B **82**, 155206 (2010).
[18] J. F. Janak, Phys. Rev. B **18**, 7165 (1978).
[19] J. P. Perdew, R. G. Parr, M. Levy, and J. L. Balduz, Jr., Phys. Rev. Lett. **49**, 1691 (1982).
[20] C.-O. Almbladh and U. von Barth, Phys. Rev. B **31**, 3231 (1985).
[21] M. Levy, J. P. Perdew, and V. Sahni, Phys. Rev. A **30**, 2745 (1984).
[22] D. P. Chong, O. V. Gritsenko, and E. J. Baerends, J. Chem. Phys. **116**, 1760 (2002).
[23] S. Kümmel and L. Kronik, Rev. Mod. Phys. **80**, 3 (2008).
[24] T. Körzdörfer, S. Kümmel, N. Marom, and L. Kronik, Phys. Rev. B **79**, 201205 (2009).
[25] T. Körzdörfer, S. Kümmel, N. Marom, and L. Kronik, Phys. Rev. B **82**, 129903(E) (2010).
[26] D. Egger, S. Weissman, S. Refaely-Abramson, S. Sharifzadeh, M. Dauth, R. Baer, S. Kümmel, J. B. Neaton, E. Zojer, and L. Kronik, J. Chem. Theory Comput. **10**, 1934 (2014).
[27] A. J. Cohen, P. Mori-Sánchez, and W. Yang, Science **321**, 792 (2008).
[28] T. Schmidt, E. Kraisler, L. Kronik, and S. Kümmel, Phys. Chem. Chem. Phys. **16**, 14357 (2014).
[29] S. Refaely-Abramson, S. Sharifzadeh, N. Govind, J. Autschbach, J. B. Neaton, R. Baer, and L. Kronik, Phys. Rev. Lett. **109**, 226405 (2012).
[30] M. Mundt, S. Kümmel, B. Huber, and M. Moseler, Phys. Rev. B **73**, 205407 (2006).
[31] M. Walter and H. Häkkinen, New J. Phys. **10**, 043018 (2008).
[32] M. Mundt and S. Kümmel, Phys. Rev. B **76**, 035413 (2007).
[33] L. Kronik and S. Kümmel, in *First Principle Approaches to Spectroscopic Properties of Complex Materials*, edited by C. D. Valentin, S. Botti, and M. Cococcioni, Topics in Current Chemistry (Springer, Berlin-Heidelberg, 2014).
[34] M. Dauth, M. Wießner, V. Feyer, A. Schöll, P. Puschnig, F. Reinert, and S. Kümmel, New J. Phys. **16**, 103005 (2014).
[35] A. Humeniuk, M. Wohlgemuth, T. Suzuki, and R. Mitrić, J. Chem. Phys. **139**, 134104 (2013).
[36] E. Runge and E. K. U. Gross, Phys. Rev. Lett. **52**, 997 (1984).
[37] K. Yabana and G. F. Bertsch, Phys. Rev. B **54**, 4484 (1996).
[38] F. Calvayrac, P.-G. Reinhard, and E. Suraud, Ann. Phys. (NY) **255**, 125 (1997).
[39] A. Castro, H. Appel, M. Oliveira, C. Rozzi, X. Andrade, F. Lorenzen, M. Marques, E. Gross, and A. Rubio, Phys. Status Solidi B **243**, 2465 (2006).
[40] M. Mundt, J. Theor. Comput. Chem. **08**, 561 (2009).
[41] U. De Giovannini, D. Varsano, M. A. L. Marques, H. Appel, E. K. U. Gross, and A. Rubio, Phys. Rev. A **85**, 062515 (2012).
[42] A. Pohl, P.-G. Reinhard, and E. Suraud, Phys. Rev. Lett. **84**, 5090 (2000).
[43] P. M. Dinh, P. Romaniello, P.-G. Reinhard, and E. Suraud, Phys. Rev. A **87**, 032514 (2013).
[44] V. Véniard, R. Taïeb, and A. Maquet, Laser Phys. **13**, 465 (2003).
[45] P. Wopperer, B. Faber, P. M. Dinh, P.-G. Reinhard, and E. Suraud, Phys. Rev. A **82**, 063416 (2010).
[46] P. Wopperer, P. M. Dinh, E. Suraud, and P.-G. Reinhard, Phys. Rev. A **85**, 015402 (2012).
[47] J. P. Perdew and A. Zunger, Phys. Rev. B **23**, 5048 (1981).
[48] T. Körzdörfer, M. Mundt, and S. Kümmel, J. Chem. Phys. **129**, 014110 (2008).
[49] D. Hofmann and S. Kümmel, J. Chem. Phys. **137**, 064117 (2012).
[50] A. Goldberg and B. W. Shore, J. Phys. B: Atom. Molec. Phys. **11**, 3339 (1978).
[51] D. E. Manolopoulos, J. Chem. Phys. **117**, 9552 (2002).

[52] S.-Y. Liu, K. Alnama, J. Matsumoto, K. Nishizawa, H. Koguchi, Y.-P. Lee, and T. Suzuki, J. Phys. Chem. A **115**, 2953 (2011).
[53] T. Carlson, P. Gerard, M. O. Krause, F. A. Grimm, and B. P. Pullen, J. Chem. Phys. **86**, 6918 (1987).
[54] D. Hofmann, T. Körzdörfer, and S. Kümmel, Phys. Rev. Lett. **108**, 146401 (2012).
[55] D. Hofmann, S. Klüpfel, P. Klüpfel, and S. Kümmel, Phys. Rev. A **85**, 062514 (2012).
[56] C. A. Ullrich, U. J. Gossmann, and E. K. U. Gross, Phys. Rev. Lett. **74**, 872 (1995).
[57] J. B. Krieger, Y. Li, and G. J. Iafrate, Phys. Rev. A **46**, 5453 (1992).
[58] For benzene the magnitude of the shift was 1.6 eV, and for pyridine it was 2.8 eV.
[59] N. Marom, F. Caruso, X. Ren, O. T. Hofmann, T. Körzdörfer, J. R. Chelikowsky, A. Rubio, M. Scheffler, and P. Rinke, Phys. Rev. B **86**, 245127 (2012).
[60] H. A. Bethe, *Handbuch der Physik* (Springer, Berlin, 1933), Vol. 24, p. 483.
[61] J. Cooper and R. N. Zare, J. Chem. Phys. **48**, 942 (1968).
[62] J. Cooper and R. N. Zare, J. Chem. Phys. **49**, 4252 (1968).
[63] Y.-i. Suzuki and T. Suzuki, J. Phys. Chem. A **112**, 402 (2008).
[64] N. Dori, M. Menon, L. Kilian, M. Sokolowski, L. Kronik, and E. Umbach, Phys. Rev. B **73**, 195208 (2006).
[65] L. Mattsson, L. Karlsson, R. Jadrny, and K. Siegbahn, Phys. Scr. **16**, 221 (1977).
[66] J. A. Sell and A. Kuppermann, Chem. Phys. **33**, 367 (1978).
[67] W. H. E. Schwarz, Angew. Chem. **45**, 1508 (2006).
[68] P. Duffy, D. P. Chong, M. E. Casida, and D. R. Salahub, Phys. Rev. A **50**, 4707 (1994).
[69] L. Kronik, A. Makmal, M. L. Tiago, M. M. G. Alemany, M. Jain, X. Huang, Y. Saad, and J. R. Chelikowsky, Phys. Status Solidi B **243**, 1063 (2006).
[70] N. Troullier and J. L. Martins, Phys. Rev. B **43**, 1993 (1991).
[71] We use LDA pseudopotentials with cutoff radii of $r_c = 1.09a_0$ for C, $r_c = 1.50a_0$ for N, and $r_c = 0.15a_0$ for H.